ELSEVIER

Journal of Structural Geology 28 (2006) 729–744

JOURNAL OF STRUCTURAL GEOLOGY

www.elsevier.com/locate/jsg

Predictive modelling of structure evolution in sandbox experiments

A.J.L. Crook [a,*], S.M. Willson [b], J.G. Yu [a], D.R.J. Owen [c]

[a] *Rockfield Software Ltd, Technium, King's Road, Prince of Wales Dock, Swansea SA1 8PH, UK*
[b] *BP America Inc., 501 Westlake Park Boulevard, Houston, TX 77079, USA*
[c] *Department of Civil Engineering, University of Wales Swansea, Singleton Park, Swansea SA2 8PP, UK*

Received 31 October 2005; received in revised form 5 February 2006; accepted 6 February 2006
Available online 29 March 2006

Abstract

In this paper a computational approach is presented that is able to forward model complex structural evolution with multiple intersecting faults that exhibit large relative movement. The approach adopts the Lagrangian method, complemented by robust and efficient automated adaptive meshing techniques, a constitutive model based on critical state concepts and global energy dissipation regularized by inclusion of fracture energy in the equations governing state variable evolution. The efficacy of the approach is benchmarked by forward simulation of two extensional analogue experiments that exhibit the development of a roll-over anticline with a series of superimposed crestal collapse graben systems. These sandbox experiments are excellent benchmarks for computational models, as both intersecting localisations with different rates of slip and large relative movement on localisations must be represented, while other complex phenomena associated with structural evolution over geological timeframes are not present.

Keywords: Fault prediction; Numerical modelling; Analogue modelling; Sand; extension

1. Introduction

Accurate reconstruction of current day geological structure has the potential to provide additional insight into the effect of the depositional history on the current geomechanical and hydrogeologic state of potential target reservoir formations and overburden. The aim is to computationally model the burial and deformational history of the sediment from initial deposition to the current day state, whilst also accounting for the reaction and transport processes occurring in the basin. This has a large potential benefit when interpreting the current-day structure, especially where the seismic imaging is poor, e.g. due to seismic interference caused by overlaying salt bodies or gas accumulations. Gaining a better appreciation of the timing of reservoir trap evolution relative to source-rock maturation and hydrocarbon migration will also impact views as to whether potential targets are oil- or gas-bearing.

Considering geomechanical modelling aspects only (the main thrust of this paper), the aim is to determine the style and distribution of the fault geometry from predictions of shear band formation and fault localization. Furthermore, fine scale gridding, below the level of seismic resolution, has the potential to allow prediction of the sub-seismic fault density, or at least identify regions with high levels of damage. Within these regions, porosity and permeability may be reduced as a consequence of grain-crushing, for example, so reducing hydrocarbon prospectivity (Fisher et al., 1999). In the context of hydrocarbon extraction from deep reservoirs mapping of these smaller faults could greatly aid decision-making of required well numbers and their placement. Interpretations of the extent of faulting also provide scenarios for determining cost-effective recoverable hydrocarbon volumes from fault-block size estimations.

The geomechanical information arising from computational modelling of the evolution of geological structure is currently qualitative rather than quantitative, due to a variety of physical and computational considerations. Physical considerations include: sizeable scale effect between laboratory tests and field scale models, the temporal variation in material constitution (lithification, creep), transient pore pressure and temperature fields, the non-uniqueness of the interpretation of the kinematic history. While computational considerations include: the effectiveness of the model in describing the onset and evolution of the localisations, the compatibility of the assumptions used to restore the geometry with the assumptions used in the forward reconstruction analysis. Resolution of these

* Corresponding author. Tel.: +44-1792-455577; fax: +44-1792-455648.
E-mail address: t.crook@rockfield.co.uk (A.J.L. Crook).

0191-8141/$ - see front matter © 2006 Elsevier Ltd. All rights reserved.
doi:10.1016/j.jsg.2006.02.002

issues requires an integrated modelling framework that properly accounts for the coupling between the reaction, transport and mechanical dynamic evolution. This necessitates computation of the simultaneous evolution of the state variables that describe the internal state of the rock formation, i.e. the material state boundary surface, rock permeability, fluid properties, the evolving rock texture and mineralogy, thermal conductivity and fault and fracture characteristics.

From the geomechanical perspective, a key computational prerequisite to developing such a framework is the accurate representation of strain localisation and the subsequent relative displacement on faults. In many cases, quantitative prediction of fault geometry necessitates accurate representation of the evolution of the material state from initial deposition to the current day conditions. Mechanical compaction, chemical compaction and long-term deviatoric creep may all play an important role during the growth of a structure. For example, porosity reduction induced by mechanical and chemical compaction, and strengthening due to cementation, may alter the position of the stress state relative to the state boundary surface, thereby either increasing or decreasing the likelihood of fault formation. In this case, the evolution of the complete state boundary surface must be represented, e.g. by extending critical state concepts, with specific models for clays and sands calibrated to enable representation of the evolution from uncemented sediment to cemented rock (Crook et al., in preparation).

The onset of localization, i.e. the formation of shear and compaction bands, arises naturally from rigorously formulated continuum constitutive models in a finite strain setting. Consequently, the inception of shear banding may be simulated in a relatively straightforward fashion. At the point of localisation initiation, however, there is a well-documented breakdown of the governing equations induced by load shedding on the discontinuity. This leads to a number of unwelcome characteristics; in particular energy dissipation in both mode-I or mode-II deformation on the localisation bands that is sensitive to the fineness and the direction of the discretisation. Consequently, strategies that either preclude, or at least mitigate, these deficiencies are essential. An overview of the commonly adopted approaches is provided in Section 2.

While procedures for prediction of the onset of localisation and the resolution of the high displacement gradients immediately following localisation are well developed, strategies suitable for resolution of large-relative-sliding that allow for gross geometric changes and topology evolution due to sedimentation and erosion have received less attention. Lagrangian, Eulerian and Arbitrary Lagrangian Eulerian (ALE) computational frameworks have all been applied in an attempt to capture the structural evolution with gross geometric changes.

The Eulerian fluid approach, for example, supplemented with appropriate techniques for fluid interface tracking, has been used in the simplified representation of the Rayleigh–Taylor instability phenomena associated with salt diapirism (Woidt, 1978; Zaleski and Julien, 1992). In this case the salt is often represented as a Newtonian or non-Newtonian fluid, which is at best a very crude approximation of complex materials that typically exhibit large deformations at finite strains dominated by viscous, plastic behaviour. Additionally, the standard Eulerian approach does not allow for accurate modelling of faulting, which is a common feature in the overburden layers.

The ALE method has also been employed for structural geology applications (Fullsack, 1995; Wissing et al., 2003; Ellis et al., 2004). However, depending on the precise formulation, ALE techniques inherit some difficulties apparent in both Eulerian and Lagrangian methodologies, e.g. for large deformation problems the ALE reduces but does not completely remove the need for remeshing. The explicit treatment of discontinuous displacement fields is also not straightforward.

The Lagrangian methodology, which is based on the reference configuration that is attached to the particles, has the advantage that: (i) free surfaces and interfaces between different phases of the system are intrinsically represented; and (ii) material state evolution is modelled directly. The complex constitutive response of rock and the initiation of structural complexity that derives from the constitutive response, e.g. fault development, are, therefore, easily incorporated. Consequently the Lagrangian methodology is most frequently employed for structural geology applications (e.g. Erickson and Jamison, 1995; Strayer and Hudleston, 1997; Nino et al., 1998; Vanbrabant et al., 1999; Erickson et al., 2001; Schultz-Ela and Walsh, 2002; Exadaktylos et al., 2003). A major disadvantage, however, is that large shear strain, e.g. diffuse straining during basin subsidence (Luo et al., 1998) or localized straining near evolving fault systems, causes excessive mesh distortion, which destroys the solution unless remedial action is undertaken, i.e. frequent rezoning or remeshing during the simulation.

The computational approach described in this work is based on the Lagrangian method, which is complemented by robust and efficient automated adaptive meshing techniques. Such methodology has been successfully employed in computational modelling of inelastic solids (Peric and Owen, 1998; Peric et al., 1999; Peric and Crook, 2004; Crook et al., in press). It is emphasized that, in addition to overcoming the difficulties caused by excessive mesh distortions, the adaptive Lagrangian formulation: (i) allows accurate tracking of the evolving localisations, as the mesh is refined in regions with high strain gradients; and (ii) provides a natural framework for computational modelling of complex interface phenomena, which may also incorporate frictional contact phenomena.

The constitutive model adopted is a single-surface, rate independent, non-associated plasticity model, based on critical state concepts. This is the simplest form of a hierarchical constitutive model specifically formulated for simulation of material evolution over geological timeframes (Crook et al., in preparation). The primary yield function is a smooth three-invariant surface that intersects the hydrostatic axis in both tension and compression. Global energy dissipation is regularized by including fracture energy in the equations governing state variable evolution (Pietruszczak and Mróz,

1981; Bažant and Oh, 1983). This approach assumes that the energy release rate for fracture growth is variable and is defined by a nonlinear resistance curve (Bažant et al., 1993) leading to a simple frictional regularization model (Crook et al., 2003; Pietruszczak and Mróz, 1981).

The efficacy of the approach is benchmarked by forward simulation of two extensional sandbox experiments in which large extensions result in the development of a roll-over anticline with a series of superimposed crestal collapse graben systems (McClay, 1990). These experiments exhibit the desirable features that: (i) the fault distribution is complex with intersecting localisations with different rates of slip; (ii) large relative movement occurs on the localisations; and (iii) other complex phenomena associated with structural evolution over geological timeframes (e.g. lithification and creep) are not present. It should also be noted that the fault distribution exhibited by these experiments is significantly more complex than observed in sandbox experiments generally adopted for computational benchmarks (e.g. Ellis et al., 2004; Nübel and Huang, 2004; Crook et al., in press).

2. Modelling strategy

The computational model adopted in this study forms part of a nonlinear finite element system that comprises procedures for both fully implicit and quasi-static explicit simulation of finite strain applications with localisation. The general procedures have been presented previously in a number of publications (e.g. Peric and Owen, 1998; Peric et al., 1999; Crook et al., 2003; Peric and Crook, 2004; Crook et al., in press) and only the details of specific interest to the current application are presented herein.

The computational approach adopted for the simulations is based on a quasi-static explicit Lagrangian method with automated remeshing triggered by a combination of distortion and accuracy considerations. The key elements of the procedures for the current application are:

1. Constitutive modelling of the sand.
2. Localisation modelling.
3. Adaptive remeshing.

2.1. Constitutive modelling of the sands

The sand constitutive model adopted for this study is a single surface rate independent non-associated elastoplastic model. It is the simplest form of the SR3 hierarchical constitutive model that combines the advantageous features of the superior sand model (Drescher and Mroz, 1997) and the sub-loading surface formulation (Hashiguchi et al., 2002). The model is flexible allowing additional sophistication, e.g. anisotropy, rate dependence, creep, etc., to be relatively easily added to the basic material characterisation. This class of constitutive model is an extension of critical state theory, which unifies the shearing and consolidation properties of soils to provide a rational hardening/softening concept that is developed around the concept of a critical state surface. This critical state surface, or residual friction surface, defines an effective stress state where unrestricted, constant-volume plastic flow occurs at constant effective stress. Therefore, unlike rudimentary constitutive models, e.g. Mohr Coulomb, the constitutive model is able to reproduce the experimentally observed response of sands in confined triaxial tests at large strains for a wide range of initial stress conditions (see Crook et al, in preparation).

The primary yield function is a smooth three-invariant surface that intersects the hydrostatic axis in both tension and compression and is defined as (Fig. 1):

$$\Phi\left(\sigma,\varepsilon_{\mathrm{v}}^{\mathrm{p}}\right)=g(\theta,p)q+(p-p_{\mathrm{t}})\tan\beta\left(\frac{p-p_{\mathrm{c}}}{p_{\mathrm{t}}-p_{\mathrm{c}}}\right)^{1/n} \tag{1}$$

where p is the effective mean stress, q is the deviatoric stress, θ is the Lode angle, p_{t} is the tensile intercept of the yield surface with the hydrostatic axis, p_{c} is the pre-consolidation pressure or compressive tensile intercept of the yield surface with the hydrostatic axis, β and n are material constants that define the shape of the yield surface in the p–q plane, and $g(\theta,p)$ is a

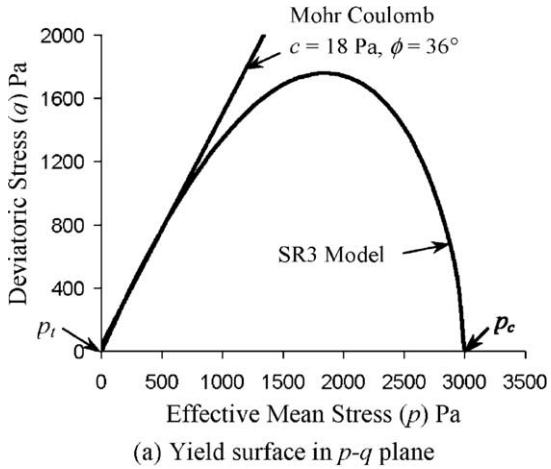

(a) Yield surface in p-q plane

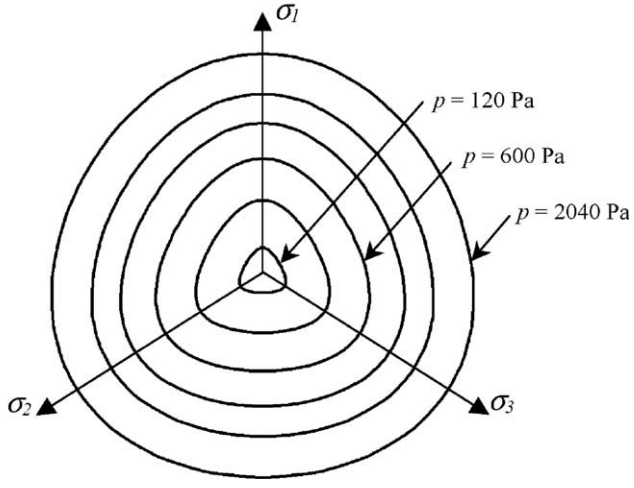

Fig. 1. Graphical representation of the initial yield surface.

function that controls the shape of the yield function in the deviatoric plane.

The evolution of the primary yield function, i.e. hardening and softening, is governed by the void ratio or plastic volumetric strain ε_v^p so that:

$$p_c = p_{c0}\exp\left[\frac{\upsilon\varepsilon_v^p}{(\lambda-\kappa)}\right] \text{ and } p_t = p_{t0}\exp\left[\frac{\upsilon(\varepsilon_v^p)_{max}}{(\lambda-\kappa)}\right] \quad (2)$$

where υ is the specific volume, λ and κ are the slopes of the normal compression line (ncl) and the unloading–reloading line (url) in the υ vs. $\ln(p)$ space, and $(\varepsilon_v^p)_{max}$ is the maximum dilatational volumetric plastic strain.

The evolution of the plastic flow is defined by a non-associated flow rule so that the plastic strain rate is defined as:

$$\dot{\varepsilon}^p = \dot{\lambda}\frac{\partial\Psi}{\partial\sigma} \quad (3)$$

where $\Psi(\sigma,\varepsilon_v^p)$ is the plastic potential, defined as:

$$\Psi\left(\sigma,\varepsilon_v^p\right) = g(\theta,p)q + (p-p_t)\tan\psi\left(\frac{p-p_c}{p_t-p_c}\right)^{1/n} \quad (4)$$

where ψ is a material parameter influencing the shape of the plastic potential surface and the plastic multiplier $\dot{\lambda}$ is consistent with the loading/unloading criterion:

$$\Phi(\sigma,q)\le 0 \quad \dot{\lambda}\ge 0 \quad \dot{\lambda}\Phi(\sigma,q) = 0 \quad (5)$$

Note that ψ is not the dilation angle, as the dilation angle is dependent on the position of the stress state relative to the yield surface. For example, in a confined triaxial test this class of constitutive model predicts maximum dilation at/near the peak load. In the post-peak regime, where inelastic deformation is confined to a shear band, dilation tends to zero once the critical state is attained within the shear band (Crook et al., in preparation).

Many expressions have been proposed for the deviatoric correction plane term $g(\theta,p)$ (see Van Eekelen (1980) for review) and a useful general expression is defined as:

$$g(\theta,p) = \left[\frac{1}{1-\beta^\pi(p)}\left(1+\beta^\pi(p)\frac{r^3}{q^3}\right)\right]^{N^\pi} \quad (6)$$

where N^π is a material constant and β^π is defined in a similar manner to Desai and Salami (1987) as:

$$\beta^\pi(p) = \beta_0^\pi\exp\left(\beta_1^\pi p\frac{p_c^0}{p_c}\right) \quad (7)$$

β_0^π and β_1^π are material constants and p_c^0 and p_c are the initial and current pre-consolidation pressure respectively, and

$$r^3 = \frac{9}{2}\mathbf{S}\cdot\mathbf{S}:\mathbf{S} = \frac{27}{2}J'_3 \quad (8)$$

where $\mathbf{S}$ is the deviatoric stress tensor and J'_3 is the third deviatoric stress invariant.

Eq. (6) is scaled so that the strength in triaxial compression directly corresponds to the strength calibrated using compressive triaxial (CTC) tests and the strength is reduced in reduced triaxial extension (RTE) tests, i.e.:

$$\text{RTE} \quad g = \left[(1+\beta^\pi)/(1-\beta^\pi)\right]^{N^\pi} \qquad \text{CTC} \quad g = 1 \quad (9)$$

The dependence of β^π on the effective mean stress enables the observed transition from the rounded-triangular yield surface at low mean stress to a circular yield surface at high mean stress (Fig. 1). Different values of N^π have been proposed and $N^\pi = 0.25$ and $0 \le \beta_0^\pi \le 0.756$ has been shown to provide a good fit for sands (Van Eekelen, 1980).

Characterising an appropriate constitutive model for simulation of the small-scale sandbox experiments performed by McClay (1990) is difficult as:

1. Limited experimental data are available for the extremely low stress range occurring in the experiments, e.g. the vertical stress due to self weight is less than 2000 Pa at 10 cm depth. Most in-depth investigations of sand properties are performed at stress levels considerably above this.
2. The constitutive response of the sand is dependent on the sample preparation technique. Experiments constructed by pouring sand have different initial grain packing to experiments constructed by sieving and sprinkling the sand. Consequently these exhibit different strength characteristics, e.g. Krantz (1991) showed that at normal stresses below 3600 Pa the peak friction angle (ϕ_p) for Fontainebleu sand varies in the range $30° < \phi_p < 45°$.

The results from several investigations using shear tests (either direct shear or ring shear) on dry sand at low normal stresses are summarized in Table 1. All researchers reported an almost linear peak strength relationship in the p–q plane for normal stresses (σ_n) in the range 400 Pa $< \sigma_n <$ 1000 Pa, and in several cases extrapolation of this surface to the $\sigma_n = 0$ Pa axis

Table 1
Material properties sand from shear tests at low normal stress

Material	Test	Normal stress range (Pa)	Grain size (μm)	c_p (Pa)	ϕ_p (°)	Sample preparation
Dry quartz: Krantz (1991)	Direct shear	600–3600	<500	520	45	Sprinkled from ca. 20 cm height
Dry quartz: Krantz (1991)	Direct shear	600–3600	<500	300	30	Poured from a large container
Dry quartz: Ellis et al. (2004)	Ring shear	500–2200	88–250	2–40	36	Sifted from ca. 20 cm height
Fontainebleu sand: Cobbold and Castro (1999)	Direct shear	300–1600	200–315	85	30	Pouring, fluidizing with compressed air, settling, consolidating via a sharp tap
Sand S1: Schellart (2000)	Direct shear	400–1000: 100–400	<400	245: >20	41.7	Slowly pouring from ca. 10 cm height
Sand S2: Schellart (2000)	Direct shear	400–1000: 100–400	90–180	230: >20	41.3	Slowly pouring from ca. 10 cm height

indicates a relatively high value of cohesion (c), e.g. Krantz (1991) suggests 300 Pa $< c <$ 520 Pa depending on the sample preparation technique. Direct shear experiments at lower normal stresses (Schellart, 2000) indicate a nonlinear peak strength relationship in the range 100 Pa $< \sigma_n <$ 400 Pa, which, when extrapolated, suggests the cohesion is very low ($<$ 20 Pa). Schellart (2000) proposed a possible explanation for the change in shape of the yield surface so that different deformation mechanisms are active at low and moderate normal stress. For low normal stresses, the individual grains in a shear zone can move over one another, leading to dilatation of the shear zone and uplift of the sediment column. For high normal stresses, this effect is suppressed and the individual grains have to slide through the irregularities.

Ellis et al. (2004), investigating the properties of dry quartz grains sifted from ca. 20 cm height with normal stresses in the range 500 Pa $< \sigma_n <$ 2200 Pa, report the shear stress vs. shear strain for a ring shear test at ca. $\sigma_n = 1800$ Pa. An initial stage of elastic deformation is followed by a stage of plastic strain-hardening that precedes the onset of failure (peak strength). Failure of the tested material corresponded to the development of a narrow shear zone, ca. 1.0–1.5 mm width, along which the arrangement of grains was perturbed and dilation had occurred. Failure was followed by a stage of load reduction, during which the shear force decreased until it reached a stable residual value.

2.2. Procedures for capturing localisation and the post-localisation response

Localization of deformation into discrete planes arises naturally in finite element simulations from the continuum constitutive response of the material, so that the inception of shear banding and the initial direction of shear bands can be simulated in a relatively straightforward fashion, e.g. by extending the work of Rudnicki and Rice (1975). Accurate representation of the propagation of localizations and evaluation of the energy dissipation in the post-localization configuration is, however, more difficult using standard continuum approaches, due to a number of well-documented issues including:

1. The direction of propagation may be severely biased by the direction of the grid lines, e.g. localizations aligned with the element edges or element diagonals.
2. Energy dissipation by both mode-I and mode-II deformation on the localisation bands is very sensitive to the fineness of the discretisation, i.e. the solutions are dependent on the *element length scale* rather than a physical *material length scale*.
3. Large shear movement on the localisations causes excessive mesh distortion, which results in termination of the solution unless the domain is remeshed.

In the context of structural geology, Erickson et al. (2001) showed that, in simulations of the initiation and reactivation of faults during movement over a rounded thrust–fault ramp, conventional finite element analysis: (i) correctly predicted bedding-parallel shear bands if the elements are initially rectangular and orientated parallel to the bedding plane, but that the number of shear bands predicted was dependent on the mesh density; and (ii) predicts no shear bands when the meshes were skewed relative to the bedding plane. Schultz-Ela and Walsh (2002), in simulations of graben formation in a brittle rock formation extending above evaporites in Canyonlands National Park, Utah, show that: (i) the predicted damage was dependent on the fineness of the finite element mesh; and (ii) localisations formed preferentially aligned with the mesh, with predictions using initially rectangular elements, or with elements slanting either forwards or backwards, producing solutions that are strongly influenced by the mesh orientation.

The many different modelling strategies proposed to overcome the first and second deficiencies may be classified based on the relative size of the finite element (h) and the width of the localization band (b) (Belytschko et al., 1988):

- Sub-h—the localisation bandwidth is smaller than the element size, e.g. embedded discontinuity methods, fracture energy, finite/discrete element methods.
- Iso-h—the element size is chosen to equal the localisation bandwidth; e.g. adaptive remeshing strategies (Zienkiewicz et al., 1998).
- Super-h—the localisation bandwidth is larger than the element size, where the width of the localization band is determined by the field equations in conjunction with a fine discretisation, e.g. non-local models (Bažant et al., 1984; Bažant and Lin, 1988), Cosserat continuum (Mühlhaus and Vardoulakis, 1987; Sluys, 1992) and gradient plasticity methods (Mühlhaus and Aifantis, 1991; Pamin, 1994).

Sub-h formulations are essential for the majority of practical rock mechanics applications as the fracture or fault width is finite, but generally very thin relative to the structural dimension, i.e. the localisation will generally be confined to a single finite element. The sub-h formulations may be further subdivided into:

- *Continuum regularization methods*, where the location and orientation of the discontinuity are not explicitly treated, e.g. the fracture energy approach (Pietruszczak and Mróz, 1981; Crook et al., 2003).
- *Discontinuity based localization modelling methods*, where the location and orientation of the discontinuity is explicitly treated, e.g. embedded discontinuity approaches (Ortiz et al., 1987; Belytschko et al., 1988; Simo et al., 1993; Oliver, 1996; Oliver et al., 2002); multi-scale approaches (Garikipati and Hughes, 2000; Miehe and Lambrecht, 2003); partition-of-unity methods (Belytschko and Black, 1999; Wells et al., 2002); the finite/discrete element method (Munjiza et al., 1995; Klerck et al., 2004).

Discontinuity-based approaches theoretically furnish higher accuracy than continuum formulations, as the additional kinematic freedom they provide should capture, with improved

accuracy, the discontinuous nature of the deformation. However, due to the complexity of the formulations, the full potential of the methodologies have yet to be demonstrated for applications involving multiple intersecting localisations with large relative movements. For these applications several outstanding issues remain to be resolved. For example, in some cases the transfer of the technology to 3-D is far from trivial and the incorporation of adaptivity with many of the proposed algorithms is not straightforward.

In the fracture energy approach, adopted in this study, the global energy dissipation is regularized by including fracture energy (G_f) as a material constant in the equations governing state variable evolution (Pietruszczak and Mróz, 1981; Bažant and Oh, 1983). This *fracture energy approach* arises from linear elastic fracture mechanics (LEFM) and has been adopted by numerous researchers for mode-I fracturing of quasi-brittle materials. Generally, the strain-softening constitutive response includes additional material constants associated with the *crack band width* and the localization is deemed to occur in the finite volume of the *crack band*, which ensures finite energy dissipation. Whilst the standard fracture energy approach has been shown to work well for mode-I fracturing of rock and concrete, the characteristic response of some rock types shows significant departure from the assumptions of LEFM. This may be approximately described by assuming that the energy release rate for fracture growth is variable and is defined by a nonlinear resistance curve (Bažant et al., 1993) instead of the constant G_f. Adoption of this concept leads to a simple frictional regularization model (Pietruszczak and Mróz, 1981; Crook et al., 2003). This fracture energy approach has the advantages that:

(a) Mesh invariance of the global energy dissipation is maintained in Sub-*h*, Iso-*h* and Super-*h* models, whereas the enhanced continuum approaches are essentially Super-*h* models.
(b) The approach may be implemented to regularize both mode-I and mode-II localization.
(c) It is straightforward to implement within any finite strain framework and for a range of constitutive models.

It must be recognized, however, that although the energy dissipation is mesh size independent the regularization method is strictly only valid for the Sub-*h* and Iso-*h* models. Furthermore, in Sub-*h* simulations the localization is limited to a single band of elements, so that the sharp gradients in the strain field will be poorly approximated if the strain field is evaluated using the standard element interpolation functions. It is also essential that the underlying element does not lock in shear and can reproduce constant volume deformation at finite strains, as this deformation state is characteristic for frictional materials sheared to the critical state at finite strains.

Notwithstanding the limitations of the regularization methodology, it has been shown to be effective in reproducing size effects in mode-II localisation for thick-walled cylinder (TWC) tests for Berea sandstone and Castlegate sandstone (Crook et al., 2003).

2.3. Adaptive solution update

The location of regions that exhibit high strain rates is continually changing during the evolution of a geological structure. Additional complexities not present in the original model may emerge, e.g. due to localisation of the deformation, altering the element density necessary for obtaining accurate solutions. Furthermore, relative deformation in regions of faulting, or large geometrical changes induced by folding, often result in excessive element distortion leading to rapid solution degradation that eventually results in premature termination of the simulation. Consequently, an adaptive mesh refinement process, driven by both accuracy and geometrical considerations, is necessary (Peric and Crook, 2004):

1. an entity based model definition,
2. an appropriate remeshing/error indicator(s) to trigger the remeshing process,
3. a strategy for defining the required mesh density based on the current material state,
4. automated topology based mesh generation tools, and
5. transfer operators to transform the material and deformational state between the original and new discretisations.

By adopting an entity based model definition all the process data, e.g. loads and constraints, are defined independently of the finite element. This is achieved by defining the geometry using a hierarchical model database constructed using points, lines, surfaces and volumes that are either imported via CAD interfaces or defined parametrically. The topology of this geometric model in then updated throughout the analysis both due to deformation of active sediments and due to activation/deactivation of material regions to represent the processes of sedimentation/erosion, respectively.

Remeshing is triggered by a combination of error estimators and mesh distortion indicators. An elementary procedure for the error estimation may be defined by the replacement of the exact values of variables and relevant derivatives of the problem by some post-processed values obtained from the available finite element solution and the problem data (Zienkiewicz and Zhu, 1987). Such procedures have been extended to elastoplastic solids, by replacing the stress based error measures with measures based on the complete material state, e.g. plastic work or plastic work rate, and have been shown to be effective for a variety of strongly nonlinear solid mechanics problems (Peric et al., 1996). Remeshing is also triggered by element distortion measures of a similar form to that proposed by Dyduch et al. (1992), whereby several measures of distortion may be specified.

The mesh refinement procedure is constructed with the objectives of: (i) minimising the local error in the finite element solution by defining new mesh densities based on the error indicators, (ii) ensuring that the mesh density is appropriate to capture the ongoing material deformation, and (iii) minimising the total number of elements in the model by constraining the allowable range of element sizes.

The adaptive procedure must not only capture the progression of the plastic deformation but also provide adequate mesh refinement in regions of possible material failure. This is achieved by adopting mesh size indicators based on the current rate of deformation or rate of plastic strain. Sharp resolution of high gradients of the state variables over a small region of the mesh is required for localisation problems, typically along a line or a surface in two- or three-dimensional problems.

After creating a new mesh, both the primary and history-dependent state variables must be transferred from the old mesh to a new mesh. In defining this process, several important aspects should be addressed (Ortiz and Quigley, 1991; Lee and Bathe, 1994; Peric et al., 1996; Rashid, 2002):

- consistency with the constitutive equations,
- requirement of equilibrium (which is fundamental for implicit FE simulation),
- compatibility of the history-dependent internal variables transfer with the displacement field on the new mesh,
- compatibility with evolving boundary conditions, and
- minimisation of the numerical diffusion of transferred state fields.

To briefly describe the transfer operation, let us define a state array ${}^{h}\Lambda$ containing the primary and state variables for mesh h at time t. Then assuming that the solution ${}^{h}\Lambda$ is within the prescribed remeshing criteria while they are violated by the solution ${}^{h}\Lambda$, a new mesh $h+1$ is generated and a new solution ${}^{h+1}\Lambda$ must to be computed. Several different strategies may be adopted to compute ${}^{h+1}\Lambda$ with the optimal procedure being dependent on the overall computational strategy and the requirement to balance accuracy and computational considerations (Peric and Crook, 2004). For quasi-static dynamic relaxation solution procedures the loading rate is sufficiently slow that the solution is directly mapped from ${}^{h}\Lambda$ to ${}^{h+1}\Lambda$ without significant loss of accuracy. This updated state ${}^{h+1}\Lambda$ is evaluated using three distinct but similar weighted least squares based procedures (e.g. Boroomand and Zienkiewicz, 1999) which map the primary variables from h nodes to $h+1$ nodes, the state variables from h gauss points to $h+1$ gauss points and the contact variables from h surfaces to $h+1$ surfaces.

3. Sandbox simulations

3.1. Description of the experimental set up

The analogue modelling experiments (McClay, 1990) were carried out in a glass-sided deformation rig (Fig. 2) with dimensions of 150 cm long, 20 cm wide and up to 20 cm deep. The sand model was constructed between the two end walls, one of which was a fixed moulded footwall block, while the other was a wall that is translated by a motor-driven worm screw at a constant displacement rate of 4.16×10^{-3} cm/s. A listric fault detachment surface formed by covering the footwall block with a plastic sheet, attached to the moving wall, translates the hanging wall. The plastic sheet simulates a weak décollement in which the hanging wall is translated over the footwall at a constant displacement rate. Two of the various geometries investigated by McClay (1990) are considered in this study, the first corresponding to experiments E37/E30 (figs. 5 and 6 in McClay, 1990) and the second corresponding to experiment E44 (fig. 7, McClay, 1990). While these experiments have the same moulded footwall geometry, in experiment E44 the apparatus was tilted so that the previously flat section now has a dip of 10°. The rigid footwall block enforces a detachment surface with a smooth constant geometry throughout the experiment, thereby confining the deformation to the hanging wall sand. McClay (1990) comments that this type of situation is found at basin margins, basement–sediment interfaces and where movement is concentrated on a single detachment fault.

Although a limited amount of frictional constraint was reported on the glass sidewalls, apparent from the curved fault traces (McClay, 1990), the visualized deformation at the side walls was taken as broadly representative of the model as a whole and is used to determine the fault sequence and overall geometry of faults. Serial sections of the completed and resin-impregnated models were used to determine the detailed final geometry of the deformation. The experiments were repeated

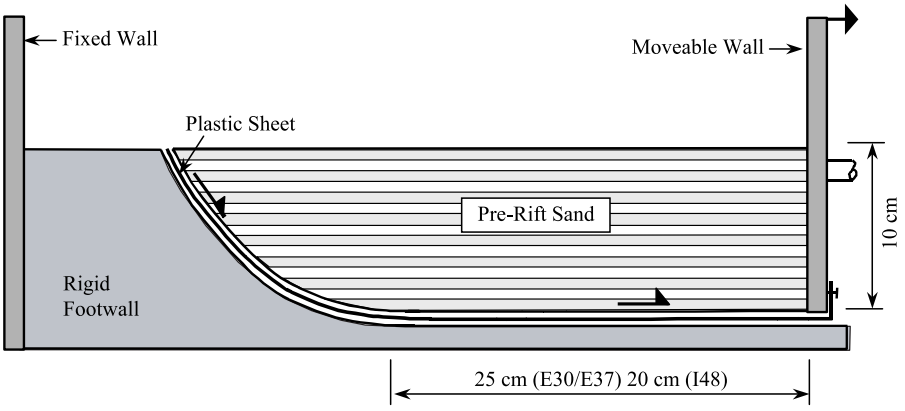

Fig. 2. Description of detachment geometry for experiments E37/E30 (McClay, 1990).

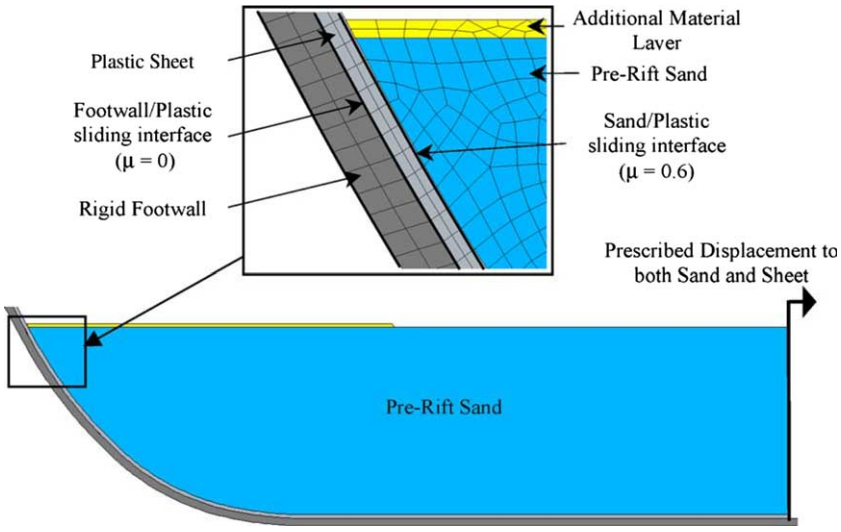

Fig. 3. Computational model for experiment E37/E30.

at least twice to ensure repeatability and similar structural style was achieved for all repeat experiments.

The McClay (1990) experiments were performed using homogeneous quartz sand (grain size ca. 300 μm) constructed by carefully sieving alternating layers of coloured sand 3–5 mm thick into the deformation rig. Sand layers were added incrementally during the extension of the model in order to maintain a constant, horizontal upper free surface and to simulate syn-rift sedimentation that infills the extensional basin.

3.2. Observed experimental response (McClay, 1990)

The fault sequence diagram for experiment E37 (Fig. 6d),[1] corresponding to 50% extension, exhibits a well established roll-over anticline with a crestal collapse graben system. The crestal collapse graben system develops due to the combination of the necessity to increase bed lengths in the upper parts of the model and the brittle nature of the constitutive response of the sand. The fault sequence diagram shows nucleation of new faults into the crestal collapse graben and superposition of younger crestal collapse grabens. The listric nature of the crestal collapse graben faults in the syn-rift sequence is evident.

In experiment E30 (Fig. 7d), where the simple listric detachment is extended to 100%, the pre-rift sequence has been translated onto the horizontal basal detachment and only syn-rift sediments are adjacent to the listric part of the fault surface. This additional relative movement on the fault surface results in superposition of crestal collapse graben systems together with a fan of synthetic listric growths in the syn-rift sequence. These synthetic listric growths form as the hanging wall migrates over the fixed footwall geometry. Successive crestal collapse grabens appear to migrate higher into the syn-rift stratigraphy with increased extension. In this experiment the synthetic crestal collapse graben bounding faults (i.e. parallel to the main detachment) are listric in the upper portions but become concave downwards at increased depth. There is, however, a tendency for these faults to merge above the little-faulted panel such that a higher-level detachment is generated, leaving a panel of unfaulted steeply dipping strata adjacent to the original fault detachment surface. Note that although the overall structural style is similar in experiments E30 and E37, the specific geometry and distribution of the faults near the pre-rift region differ in the two experiments. This gives an indication of the potential dependence of specific fault distributions on the initial density distribution of the sand.

For experiment E44, where the basal detachment dip in the direction of extension is 10°, the pre-rift sequence drops below the original elevation so that each successive layer of syn-rift sediment overlays the complete domain (Fig. 8f). The superposition of crestal collapse grabens is also very marked in this experiment. A listric fan system, synthetic and parallel to the main detachment geometry, is well developed such that a distinctive panel of unfaulted strata is carried down the main detachment. The fault sequence diagram shows the strongly listric growth shape of the crestal collapse graben bounding faults in the syn-rift sequence and that younger faults are progressively initiated towards the centre of the crestal graben.

3.3. Model description

The computational model (Fig. 3) corresponds to a 2-D plane strain section where the moulded footwall, plastic sheet and sand are represented as separate bodies. As the precise geometry of the moulded footwall was not provided it is scaled from the figures in McClay (1990). The moulded footwall is represented as a rigid body and the plastic sheet is represented as an elastic body. The pre-rift sand is represented as a single layer and the syn-rift sand is represented by additional material

[1] The figures corresponding to the experimental results (Figs. 6d, 7d and 8f) are shown out of sequence to allow direct comparison with the computational predictions.

Table 2
Elastic properties

Parameter	Value
Density (ρ)	1.56 g/cm^3
Young's modulus (E)	75,000 Pa
Poisson's ratio (ν)	0.2

Table 3
Material properties defining the initial yield surface

Parameter	Value
Initial tensile intercept (p_{t0})	-20 Pa
Initial compressive intercept (p_{c0})	3000 Pa
Parameter (β)	60°
Parameter (ψ)	50°
Deviatoric plane parameter (N^{π})	0.25
Deviatoric plane parameter (β_0^{π})	0.6
Deviatoric plane parameter (β_1^{π})	7×10^{-4}

Table 4
Material properties for evolution of the yield surface

Parameter	Value
Initial specific volume (v)	1.67
$\lambda-\kappa$	0.48
Characteristic length (l_c)	1.5 mm

layers that are activated after each incremental displacement of the distal moveable wall. The new material layers are defined such that the new top surface is flat while the bottom surface is continuous with the top surface of the previously active sand. A contact interface model is used to represent the interaction between the footwall and the plastic sheet and the plastic sheet and the sand. A frictionless condition for the footwall/sheet interface and a Coulomb friction interface model with friction coefficient $\mu=0.3$ is assumed for the sheet/sand interface. The translation of the moveable wall is represented by prescribing the motion of both the boundary of the sand and the plastic sheet on the distal edge of the model.

A multi-stage analysis procedure is adopted where an initial equilibrium state is first achieved due to the self-weight of the sand and then the rigid wall and sheet are then translated 15 mm using a ramp function. After each 15 mm movement a new material layer representing newly deposited syn-rift sediment is activated. To simplify this activation process for experiments E30/E37, where the elevation of the top surface of the pre-rift sand in the region of the rigid wall remains unchanged, this new layer is 0.5 mm higher in elevation than the top surface of the previous layer. This process is thereafter repeated sequentially. No initial imperfections or discontinuity seeding is used, so that the localisation pattern arises naturally from the imposed boundary conditions and the constitutive behaviour of the modelled sand.

Adaptive remeshing is triggered via a measure of the element distortion. The lower bound target element size is controlled by the plastic strain rate and an upper bound mesh-coarsening criterion is defined as a function of the effective plastic strain. The minimum element size is set to 1.0 mm, with

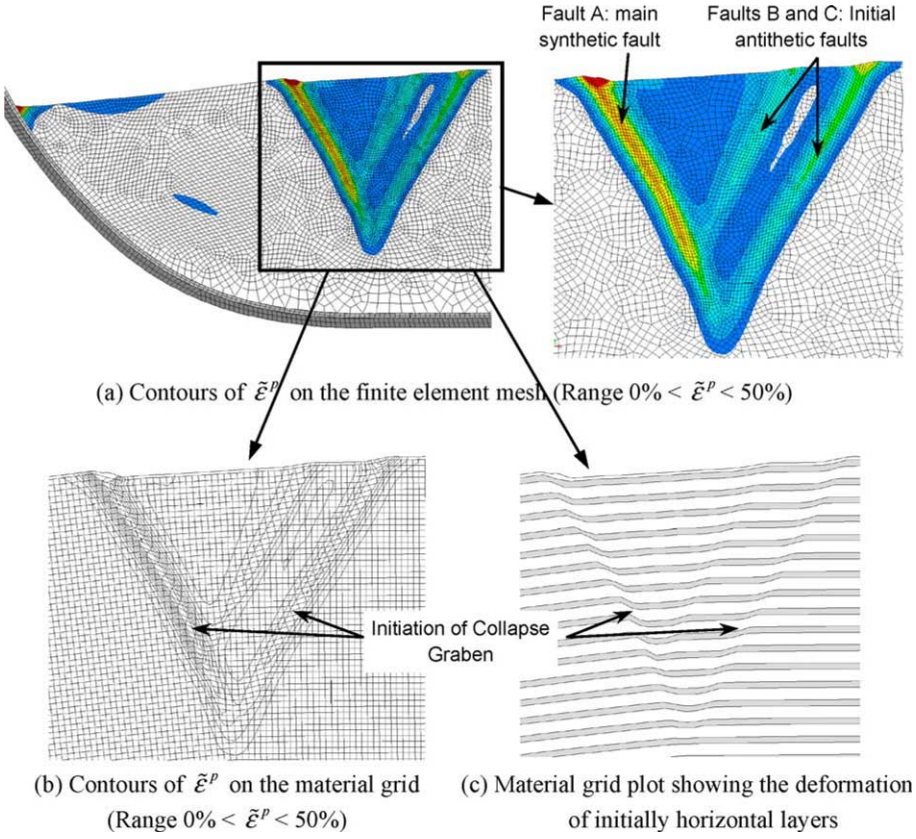

Fig. 4. Configuration of the pre-rift sand after 15 mm extension.

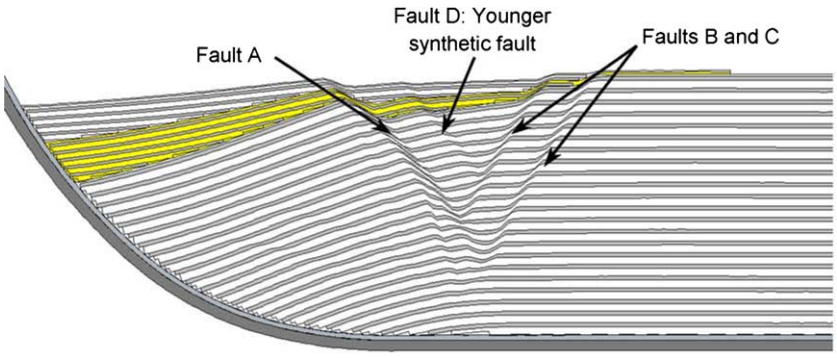

(a) Layer deformation plot show pre-rift sand and two layers of syn-rift sand

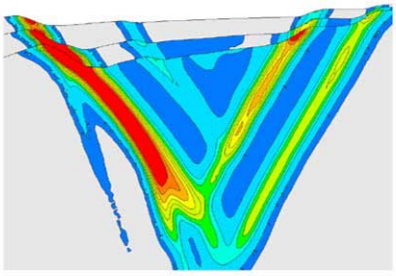

(b) Contours of $\tilde{\varepsilon}^p$ (Range 0% < $\tilde{\varepsilon}^p$ < 100%)

Fig. 5. Configuration of the pre-rift sand after 45 mm extension.

a maximum element size of 2.0 mm in active/previously active regions and 5.0 mm in regions with low activity.

No triaxial or hydrostatic test data is provided in the McClay (1990) paper at the stress levels associated with the sandbox tests. Based on the observed response, therefore, the elastic properties are defined in Table 2, the initial yield surface is set (Tables 2 and 3) so that it coincides with a Mohr–Coulomb surface with $c = 18$ Pa, $\phi = 36°$ at low values of p and the compressive intercept is set at 3000 Pa (Fig. 1). This provides a simple characterisation which, together with the hardening/softening data (Table 4) and global energy dissipation regularized using the generalisation of the fracture energy approach, results in a relative brittle response in the near surface sand in the sandbox experiment, tending to a more ductile response at the base of the model.

A material grid is used to aid visualisation of the deformation in all of the examples presented. This is a regular grid, initially aligned with the horizontal and vertical axes, which is superimposed on the sand discretisation in the undeformed configuration and subsequently enforced to follow the deformation. Plotting the current configuration of the grid then identifies relative movement of the sand. The grid is also displayed using stripes that are analogous to the coloured sand utilized in the experiments. The syn-rift sand is shown with thinner strip thickness than the pre-rift sand and different colours identify alternate syn-rift layers.

3.4. Computational results for the E30/E37 experiment

The configuration at 15 mm extension (Fig. 4) shows that a crestal collapse graben is predicted to initiate with larger relative movement on the synthetic fault (Fault A) relative to the two antithetic faults (Faults B and C). Three zoom views are provided, which show contours of effective plastic strain ($\tilde{\varepsilon}^p$) on the mesh discretisation, the deformation of the material grid and a horizontal layer deformation plot derived from the deformed material grid. The material grid plots show that the shear deformation is largely confined to the fault regions, although a low level of plasticity is pervasive within the graben. As commented by McClay (1990), this collapse graben is inevitable when extension decreasing with depth from the free surface is applied to a quasi-brittle material.

The configuration at 45 mm extension (Fig. 5) shows that the original synthetic and antithetic faults are still active and that a younger synthetic fault (Fault D) has formed above the graben. All four faults have propagated into the new syn-rift material layers that were activated after 15 and 30 mm extension. The zoom view of contours shows that the highest relative movement occurs on the synthetic fault (Fault A).

The listric nature of the crestal collapse synthetic bounding fault in the syn-rift sequence is clearly evident at 75 mm extension (Fig. 6a). Steeply dipping synthetic faults have also formed both on and slightly ahead of the main synthetic fault. At 105 mm extension (Fig. 6b) younger faults have initiated above the original graben and a new graben feature has formed superimposed on the original structure. At this stage the bounding faults for the original graben are almost inactive in the pre-rift material.

Comparison of the predictions for 135 mm extension (Fig. 6c) with the fault sequence diagram for experiment E37

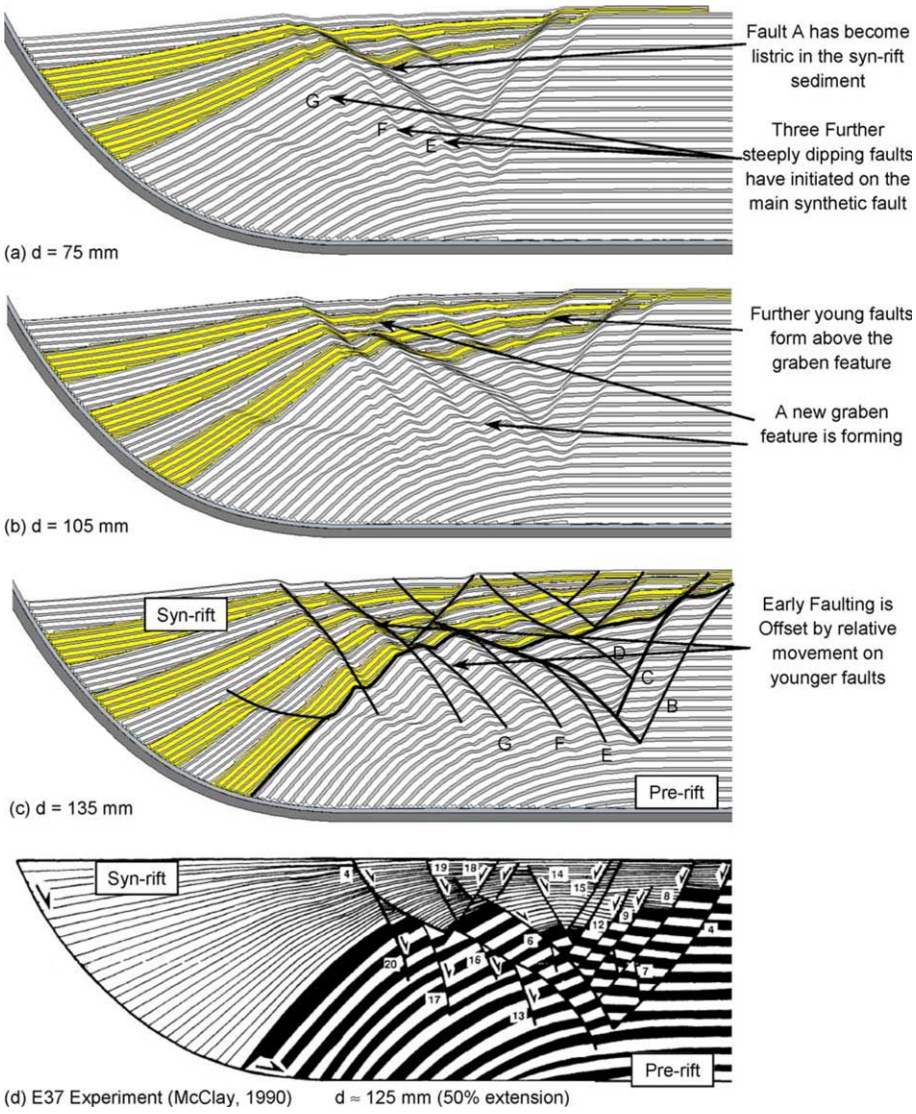

Fig. 6. Comparison of computational predictions and the experimental observations for experiment E37.

(Fig. 6d) shows that the major structural features observed experimentally are also reproduced in the model, namely:

1. A well established roll-over anticline is created with a crestal collapse graben system.
2. The synthetic bounding faults that are listric in the syn-rift sand and trend in shape to concave downwards nearer the basal detachment.
3. Newer faults have initiated within the main crestal collapse graben.
4. Steeply dipping faults exist below the synthetic bounding fault.
5. Younger superimposed crestal collapse grabens are formed within the main collapse graben.
6. The listric nature of the crestal collapse graben faults in the syn-rift sequence is evident.

A fault sub-parallel to the main detachment, but with low relative movement, is predicted in the model but not evident in the experiment. Furthermore, the listricity of the faults in the syn-rift sediment is predicted to be lower than observed in the experiment. These discrepancies are likely to be due to differences in the modelled and true constitutive response of the sand. Due to the paucity of experimental data at these low stress levels, however, this cannot be readily confirmed.

The sequence of plots for extensions of 150 mm (Fig. 7a), 180 mm (Fig. 7b) and 210 mm (Fig. 7c) show that the computational predictions have many of the characteristics observed in the experiments (Fig. 7d)[2] and reported by McClay (1990), e.g.:

1. The panel of relatively unfaulted steeply dipping pre- and syn-rift sediments that exists adjacent to the basal listric detachment.
2. With continued extension, the main fault activity remains near the listric detachment region, with new graben features being continually superimposed on the existing structure.

[2] Note that the experiment has a greater total extension than the simulation.

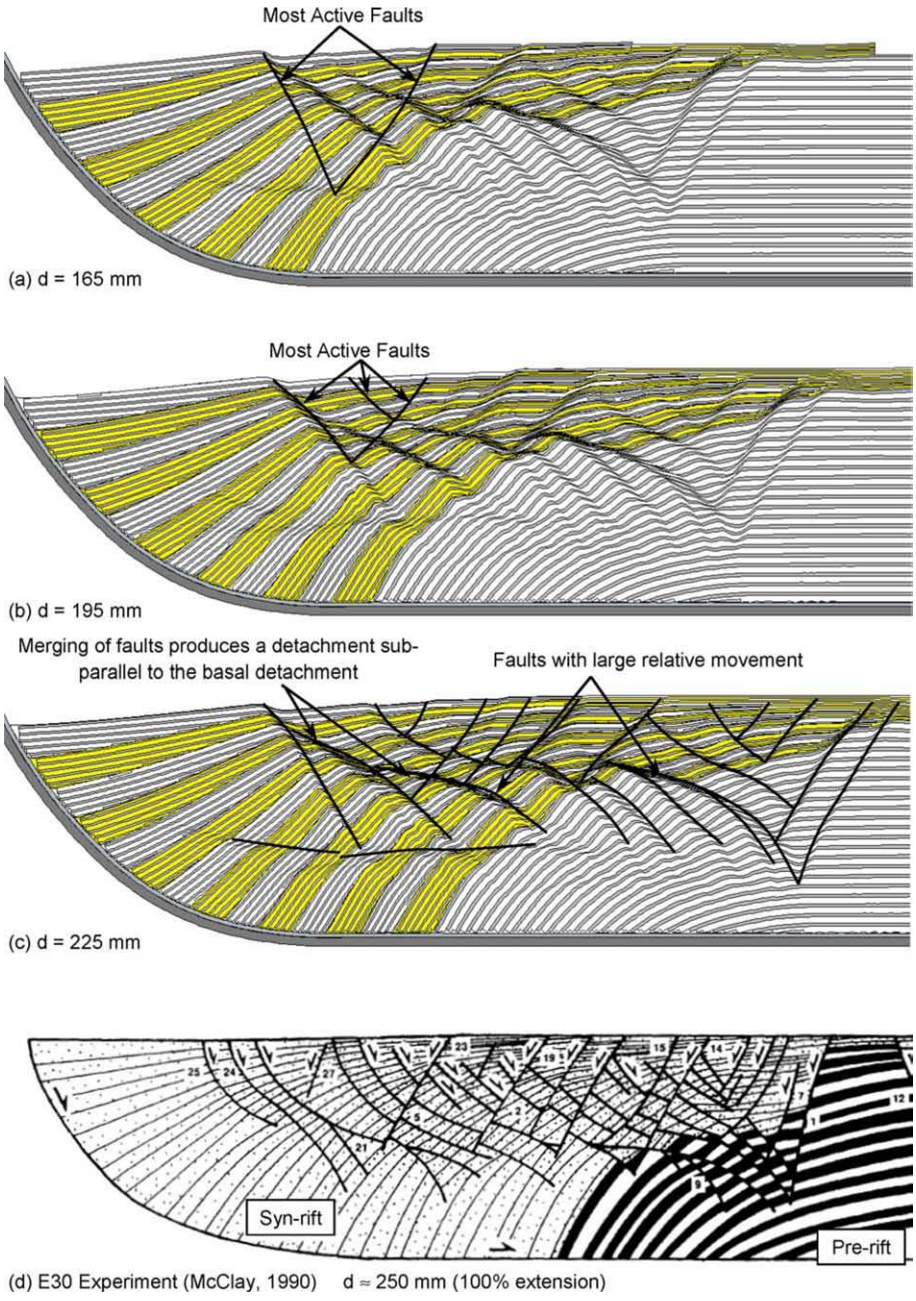

Fig. 7. Comparison of computational predictions and the experimental observations for experiment E30.

As the structure is transported away from this region, via relative displacement of the hanging wall over the footwall, the older faults become inactive. This may be seen by plotting the incremental displacement in the computational model, which shows that at an extension of 210 mm the original graben feature is translating under rigid body motion (not shown).

3. The synthetic crestal collapse graben bounding faults are listric in the upper portions but become concave downwards at increased depth. In the computational model, these faults are initially relatively steeply dipping, but are subsequently progressively rotated due to relative movement of underlying sediment over the basal detachment. Extension of these faults into syn-rift layers that are deposited subsequent to the initial fault initiation follows trajectories closer to the original fault dip, leading to the listric geometry in the near surface segment of the fault.
4. Some of the listric synthetic faults merge to produce a higher-level detachment sub-parallel to the basal detachment surface. In both the experiment and the model, there is a tendency for these faults to be subsequently offset by relative movement on antithetic faults.

3.5. Computational results for the E44 experiment (tilted base)

The configuration at 45 mm extension (Fig. 8a) shows that, as in the E30 simulation, an initial crestal collapse graben

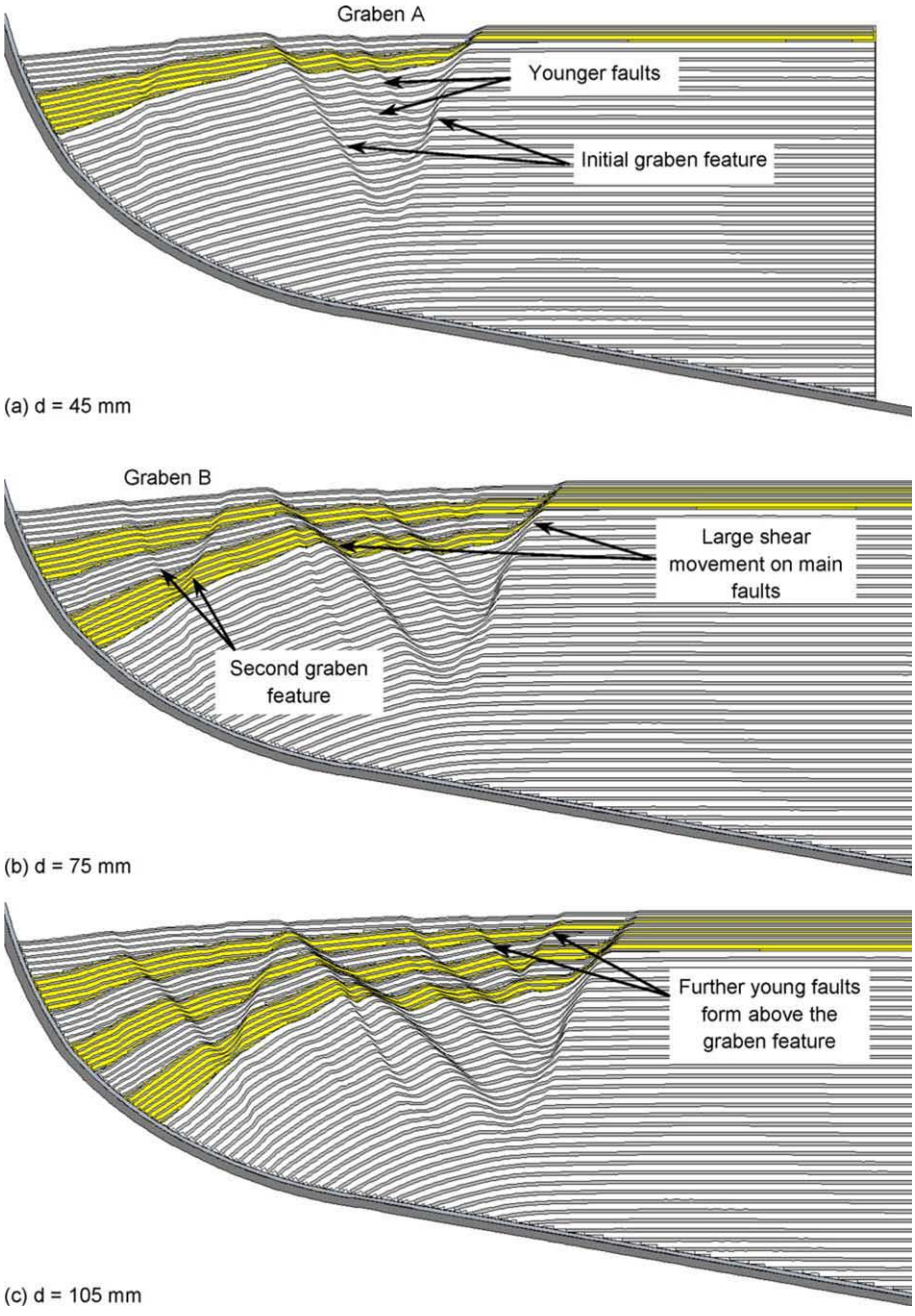

Fig. 8. Comparison of computational predictions and the experimental observations for experiment E44.

(Graben A) is predicted to initiate just distal of the intersection of the listric detachment with the inclined detachment. This graben contains two younger synthetic faults.

At 75 mm extension (Fig. 8b), further relative movement on the basal detachment causes rotation of the synthetic fault in the pre-rift sand and, therefore, widening of the graben. This in turn causes large relative slip on the faults bounding the graben, which is evident from the elevation offset of the first syn-rift layer. A second graben feature (Graben B) is also evident closer to the listric basal detachment. Continued extension results in further widening of the original graben, so that the bounding faults remain active in both the pre-rift and syn-rift sand and younger faults are formed above the graben (Fig. 8c).

At 165 mm extension (Fig. 8d), the bounding faults of the Graben A are inactive and a younger graben (Graben C) is superimposed on Graben B. The synthetic bounding fault of Graben B is listric and sub-parallel to the basal detachment surface, while the bounding antithetic fault is more vertical. This is due to rotation of the sediment necessary to accommodate the extension of the model. The synthetic fault for Graben B is still active and propagates through all of the newly deposited syn-rift layers, whereas the antithetic fault is now inactive.

Comparison of the configuration at 225 mm extension (Fig. 8) with the experimental fault sequence diagram (Fig. 8f) shows that, although the specific fault geometries differ, the

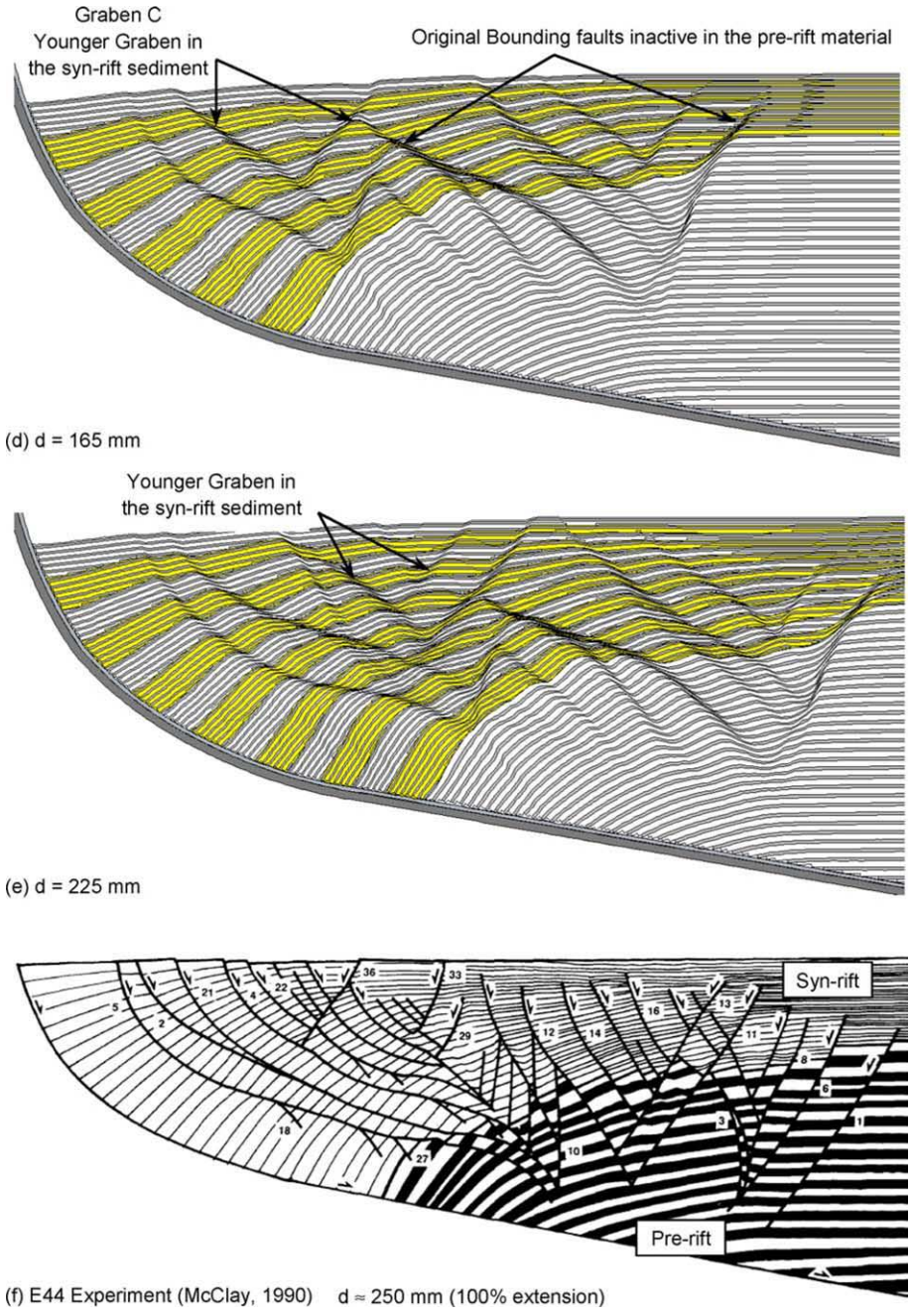

Fig. 8 (*continued*)

following generic overall features are evident in both the experiment and the simulation:

1. A superposition of crestal collapse grabens occurs in the syn-rift sediment above, and in the neighbourhood of, the listric basal detachment.
2. A well developed listric fan system forms, synthetic and parallel to the basal detachment geometry, with a panel of unfaulted steeply dipping strata which is carried down the basal detachment.
3. Listric crestal collapse graben bounding faults exist in the syn-rift sequence and younger faults are progressively initiated towards the centre of the crestal graben.
4. The faulted structures that have been transported down the inclined section of the basal detachment are inactive and do not propagate to the surface of the newly deposited syn-rift sediments.

Although the model reproduces the characteristic response, the density of the predicted faulting is lower than observed in the experiment. This discrepancy is probably due to a combination of factors, e.g. heterogeneities in the experiment not present in the model, differences in the true and model constitutive response, differences in the kinematic freedom (small grain size vs. relatively large element size), etc. Consequently, detailed further investigation is required to

resolve the relative contribution of these factors to the discrepancy.

4. Conclusions

A computational approach is presented that is able to forward model complex structural evolution with multiple intersecting faults that exhibit large relative movement. The approach adopts the Lagrangian method, complemented by robust and efficient automated adaptive meshing techniques, a constitutive model based on critical state concepts and global energy dissipation regularized by inclusion of fracture energy in the equations governing state variable evolution.

The efficacy of the approach is benchmarked by forward simulation of two extensional sandbox experiments that exhibit complex fault development including a series of superimposed crestal collapse graben systems. It is emphasized that no initial perturbations or fault seeding is imposed and that the structure evolves solely from the prescribed movement on the basal detachment. Comparison of the predicted and experimental configurations shows that, although the specific fault geometries differ, many common features are evident, including: (i) the development of an initial collapse graben; (ii) initiation of younger faults within the bounding faults of the graben; (iii) the superposition of crestal collapse grabens in the syn-rift sediment; (iv) creation of synthetic crestal collapse graben bounding faults that are listric in the upper portions but become concave downwards at increased depth; and (v) the development of a listric fan system, synthetic and parallel to the basal detachment geometry.

While the simulations reproduce the style of structure evolution observed in the experiments, they suffer from deficiencies, such as: (i) it can be argued that the energy regularisation is unsophisticated and that a more rigorous formulation would be more appropriate; (ii) the diffusion of the material state caused by the mapping phase of the adaptive remeshing procedure results in more diffuse localisations in the simulation than observed in the experiment; and (iii) the discretisations are finer than would be computationally expedient for simulation of 3-D field-scale applications. Sub-h localisation formulations, in conjunction with enhanced adaptive remeshing strategies in which the localisation is treated as an explicit entity, potentially offer a remedy for both these deficiencies and are a subject of ongoing research.

Acknowledgements

The authors would like to thank BP America Inc. for permission to publish this work and for funding some aspects of this research.

References

Bažant, Z.P., Lin, F., 1988. Nonlocal smeared cracking model for concrete fracture. Journal of Structural Engineering ASCE 114, 2493–2510.

Bažant, Z.P., Oh, B., 1983. Crack band theory for fracture of concrete. RILEM Materials and Structures 16, 155–177.

Bažant, Z.P., Belytschko, T.B., Chang, T., 1984. Continuum theory for strain-softening. Journal of Engineering Mechanics ASCE 110, 1666–1692.

Bažant, Z.P., Lin, F., Lippmann, H., 1993. Fracture energy release and size effect in borehole breakout. International Journal for Numerical and Analytical Methods in Geomechanics 17, 1–14.

Belytschko, T., Black, T., 1999. Elastic crack growth in finite elements with minimal remeshing. International Journal for Numerical Methods in Engineering 45, 601–620.

Belytschko, T., Fish, J., Engelman, B.E., 1988. A finite element with embedded localization zones. Computer Methods in Applied Mechanical Engineering 70, 59–89.

Boroomand, B., Zienkiewicz, O.C., 1999. Recovery procedures in error estimation and adaptivity. Part II: adaptivity in nonlinear problems in elasto-plasticity behaviour. Computer Methods in Applied Mechanical Engineering 176, 127–146.

Cobbold, P.R., Castro, L., 1999. Fluid pressure and effective stress in sandbox models. Tectonophysics 301, 1–19.

Crook, A.J.L., Owen, D.R.J., Willson, S.M., Yu, J.G., 2006. Benchmarks for the evolution of shear localisation with large relative sliding in frictional materials. Computer Methods in Applied Mechanics and Engineering, in press.

Crook, A.J.L., Yu, J.G., Willson, S.M., Owen, D.R.J., in preparation. Constitutive modelling of sands and sandstones in hydrocarbon reservoirs.

Crook, T., Willson, S.M., Yu, J.G., Owen, D.R.J., 2003. Computational modelling of the localized deformation associated with borehole breakout in quasi-brittle materials. Journal of Petroleum Science and Engineering 38, 177–186.

Desai, C.S., Salami, M.R., 1987. A constitutive model and associated testing for soft rock. International Journal of Rock Mechanics and Mining Sciences 24, 299–307.

Drescher, A., Mroz, Z., 1997. A refined superior sand model. In: Pietruszcak, S., Pande, G.N. (Eds.), Numerical Methods in Geomechanics NUMOG VI. Balkema, Rotterdam, pp. 21–26.

Dyduch, M., Habraken, A.M., Cescotto, S., 1992. Automatic adaptive remeshing for numerical simulations of metal forming. Computer Methods in Applied Mechanical Engineering 101, 283–298.

Ellis, S., Schreurs, G., Panien, M., 2004. Comparisons between analogue and numerical models of thrust wedge development. Journal of Structural Geology 26, 1659–1675.

Erickson, S.G., Jamison, W.R., 1995. Viscous-plastic finite-element models of fault-bend folds. Journal of Structural Geology 17, 561–573.

Erickson, S.G., Strayer, L.M., Suppe, J., 2001. Initiation and reactivation of faults during movement over a thrust–fault ramp: numerical mechanical models. Journal of Structural Geology 23, 11–23.

Exadaktylos, G.E., Vardoulakis, I., Stavropoulou, M.C., Tsombos, P., 2003. Analogue and numerical modelling of normal fault patterns produced due to slip along a detachment zone. Tectonophysics 376, 117–134.

Fisher, Q.J., Casey, M., Clennell, M.B., Knipe, R.J., 1999. Mechanical compaction of deeply buried sandstones of the North Sea. Marine and Petroleum Geology 16, 605–618.

Fullsack, P., 1995. An arbitrary Lagrangian–Eulerian formulation for creeping flows and applications to tectonic models. Geophysical Journal International 120, 1–23.

Garikipati, K., Hughes, T.J.R., 2000. A variational multiscale approach to strain localization-formulation for multi-dimensional problems. Computer Methods in Applied Mechanical Engineering 188, 39–60.

Hashiguchi, K., Saitoh, K., Okayasu, T., Tsutsumi, S., 2002. Evaluation of typical conventional and unconventional plasticity models for prediction of softening behaviour of soils. Géotechnique 52, 561–578.

Klerck, P.A., Sellers, E.J., Owen, D.R.J., 2004. Discrete fracture in quasi-brittle materials under compressive and tensile stress states. Computer Methods in Applied Mechanical Engineering 193, 3035–3056.

Krantz, R.W., 1991. Measurements of friction coefficients and cohesion for faulting and fault reactivation in laboratory models using sand and sand mixtures. Tectonophysics 188, 203–207.

Lee, N.-S., Bathe, K.-J., 1994. Error indicators and adaptive remeshing in large deformation finite element analysis. Finite Elements in Analysis and Design 16, 99–139.

Luo, X., Vasseur, G., Pouya, A., Lamoureux-Var, V., Poliakov, A., 1998. Elastoplastic deformation of porous media applied to the modelling of compaction at basin scale. Marine and Petroleum Geology 15, 145–162.

McClay, K.R., 1990. Extensional fault systems in sedimentary basins: a review of analogue model studies. Marine and Petroleum Geology 7, 206–233.

Miehe, C., Lambrecht, M., 2003. A two-scale finite element relaxation analysis of shear bands in non-convex inelastic solids: small-strain theory for standard dissipative materials. Computer Methods in Applied Mechanical Engineering 192, 473–508.

Mühlhaus, H.-B., Aifantis, E.C., 1991. A variational principle for gradient plasticity. International Journal of Solids and Structures 28, 845–857.

Mühlhaus, H.-B., Vardoulakis, I., 1987. The thickness of shear bands in granular materials. Géotechnique 37, 845–857.

Munjiza, A., Owen, D.R.J., Bićanić, N., 1995. A combined finite-discrete element method in transient dynamics of fracturing solids. Engineering Computations 12, 145–174.

Nino, F., Philip, H., Chery, J., 1998. The role of bed-parallel slip in the formation of blind thrust faults. Journal of Structural Geology 20, 503–516.

Nübel, K., Huang, W., 2004. A study of localized deformation pattern in granular media. Computer Methods in Applied Mechanical Engineering 193, 2719–2743.

Oliver, J., 1996. Modelling strong discontinuities in solid mechanics via strain softening constitutive equations. Part 1: fundamentals. International Journal for Numerical Methods in Engineering 39, 3575–3600.

Oliver, J., Huespe, A.E., Pulido, M.D.G., Chaves, E., 2002. From continuum mechanics to fracture mechanics: the strong discontinuity approach. Engineering Fracture Mechanics 69, 113–136.

Ortiz, M., Quigley IV., J., 1991. Adaptive mesh refinement in strain localization problems. Computer Methods in Applied Mechanical Engineering 90, 781–804.

Ortiz, M., Leroy, Y., Needleman, A., 1987. A finite element method for localized failure analysis. Computer Methods in Applied Mechanical Engineering 61, 189–214.

Pamin, J.K., 1994. Gradient-dependent plasticity in numerical simulation of localization phenomena. Ph.D. thesis, Delft Univ. Tech.

Peric, D., Crook, A.J.L., 2004. Computational strategies for predictive geology with reference to salt tectonics. Computer Methods in Applied Mechanical Engineering 193, 5195–5222.

Peric, D., Owen, D.R., 1998. Finite element applications to the nonlinear mechanics of solids. Reports on Progress in Physics 61, 1495–1574.

Peric, D., Hochard, C., Dutko, M., Owen, D.R.J., 1996. Transfer operators for evolving meshes in small strain elasto-plasticity. Computer Methods in Applied Mechanical Engineering 137, 331–344.

Peric, D., Vaz Jr., M., Owen, D.R.J., 1999. On adaptive strategies for large deformations of elasto-plastic solids at finite strains: computational issues and industrial applications. Computer Methods in Applied Mechanical Engineering 176, 279–312.

Pietruszczak, S., Mróz, Z., 1981. Finite element analysis of deformation of strain softening materials. International Journal for Numerical Methods in Engineering 17, 327–334.

Rashid, M.M., 2002. Material state remapping in computational solid mechanics. International Journal for Numerical Methods in Engineering 55, 431–450.

Rudnicki, J.W., Rice, J.R., 1975. Conditions for the localisation of deformation in pressure-sensitive dilatant materials. Journal of Mechanical Physics and Solids 23, 371–394.

Schellart, W.P., 2000. Shear test results for cohesion and friction coefficients for different granular materials: scaling implications for their usage in analogue modeling. Tectonophysics 324, 1–16.

Schultz-Ela, D.D., Walsh, P., 2002. Modelling of grabens extending above evaporites in Canyonlands National Park, Utah. Journal of Structural Geology 24, 247–275.

Simo, J.C., Oliver, J., Armero, F., 1993. An analysis of strong discontinuities induced by softening relations in rate-independent solids. Computational Mechanics 12, 277–296.

Sluys, L.J., 1992. Wave propagation, localisation and dispersion in softening solids. Ph.D. thesis, Delft Inst. Tech.

Strayer, L.M., Hudleston, P.J., 1997. Numerical modelling of fold initiation at thrust ramps. Journal of Structural Geology 19, 551–566.

Van Eekelen, H.A.M., 1980. Isotropic yield surfaces in three dimensions for use in soil mechanics. International Journal for Numerical and Analytical Methods in Geomechanics 4, 89–101.

Vanbrabant, Y., Jongmans, D.M., Hassani, R., Bellino, D., 1999. An application of two-dimensional finite-element modelling for studying the deformation of the Variscan fold-and-thrust belt (Belgium). Tectonophysics 309, 141–159.

Wells, G.N., Sluys, L.J., de Borst, R., 2002. Simulating the propagation of displacement discontinuities in a regularised strain-softening medium. International Journal for Numerical Methods in Engineering 53, 1235–1256.

Wissing, S.B., Ellis, S., Pfiffner, O.A., 2003. Numerical models of Alpine-type cover nappes. Tectonophysics 367, 145–172.

Woidt, W.-D., 1978. Finite element calculations applied to salt dome analysis. Tectonophysics 50, 369–386.

Zaleski, S., Julien, P., 1992. Numerical simulation of Rayleigh–Taylor instability for single and multiple salt diapirs. Tectonophysics 206, 55–69.

Zienkiewicz, O.C., Zhu, J.Z., 1987. A simple error estimator and adaptive procedure for practical engineering analysis. International Journal for Numerical Methods in Engineering 24, 337–357.

Zienkiewicz, O.C., Pastor, M., Huang, M., 1998. Softening, localization and adaptive remeshing. Capture of discontinuous solutions. Computational Mechanics 17, 98–106.